

One-Dimensional Carbon–Sulfur Composite Fibers for Na–S Rechargeable Batteries Operating at Room Temperature

Tae Hoon Hwang,[†] Dae Soo Jung,[†] Joo-Seong Kim,[†] Byung Gon Kim,[†] and Jang Wook Choi^{*,†,‡}

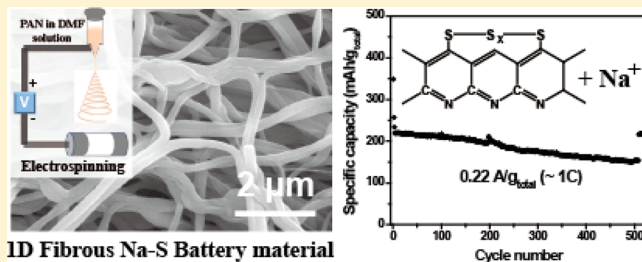
[†]Graduate School of EEWs (WCU) and [‡]KAIST Institute NanoCentury, Korea Advanced Institute of Science and Technology (KAIST), 291 Daehak-ro, Yuseong-gu, Daejeon 305-701, Republic of Korea

 Supporting Information

ABSTRACT: Na–S batteries are one type of molten salt battery and have been used to support stationary energy storage systems for several decades. Despite their successful applications based on long cycle lives and low cost of raw materials, Na–S cells require high temperatures above 300 °C for their operations, limiting their propagation into a wide range of applications. Herein, we demonstrate that Na–S cells with solid state active materials can perform well even at room temperature when sulfur-containing carbon composites generated from a simple thermal reaction were used as sulfur

positive electrodes. Furthermore, this structure turned out to be robust during repeated (de)sodiation for ~500 cycles and enabled extraordinarily high rate performance when one-dimensional morphology is adopted using scalable electrospinning processes. The current study suggests that solid-state Na–S cells with appropriate atomic configurations of sulfur active materials could cover diverse battery applications where cost of raw materials is critical.

KEYWORDS: Composite, electrospinning, nanofiber, sodium-ion battery, sulfur



Conventional sodium–sulfur (Na–S) batteries are one type of molten salt battery in which the molten phases of both active materials are separated by beta-alumina solid electrolytes with high Na ion conductivities.^{1–3} During discharge, Na ions migrate from the molten sodium to the molten sulfur through the solid electrolyte generating a cell voltage about 2 V. Since their initial development by Ford Motor in the 1960s, Na–S batteries have been used largely for grid scale storage applications utilizing excellent lifetime and abundance of raw materials. However, preservation of the molten state and moderate Na diffusion in the solid electrolyte require high-temperature operating conditions typically above 300 °C, rendering the overall system ineffective from an energy usage viewpoint.^{1–4}

Meanwhile, commercial products in the 1990s began to incorporate lithium ion batteries (LIBs), and since then LIBs have supported a wide range of small-scale applications represented by portable electronic devices. However, the increasing demand for grid scale energy storage systems (ESS's) has built the consensus that sodium ion batteries (SIBs) may be more suitable for those applications in which price and abundance of raw materials are more critical for widespread use.^{5,6} Based on this motivation, the battery community has recently found many promising SIB electrode materials. However, SIBs still suffer from inferior electrochemical performance compared to those of LIBs mainly due to the relatively large sizes of Na ions and resultant less efficient Na diffusion within the crystal structures of active materials.

Focusing on the great potential of SIBs toward ESS applications, in the present investigation, we revisit Na–S batteries but endeavor to develop high-performance Na–S cells operating at room temperature. For this, we adopt an approach from recent research on analogous Li–S cells in which various sulfur electrode designs have addressed conventional critical issues including shuttling effect of polysulfides and low electric conductivity of sulfur.^{7,8} In particular, we used the composites generated from thermal reactions between elemental sulfur and conducting polymers for Na–S cells. These electrode structures contain sulfur nanodomains and sulfur–carbon bonds in the conductive carbon matrices and turn out to be stable during repeated cycles. Furthermore, in pursuit of high rate capability, which has been challenging in both the conventional Na–S and Li–S cells, a one-dimensional (1D) fibrous morphology was developed by employing a scalable electrospinning process. The current study suggests that the sulfur composite electrode with appropriate internal nanostructures can pave a way for highly functional room temperature Na–S batteries. Although some room-temperature Na–S batteries have been reported, they focused on development of robust electrolytes,^{4,9–11} not electrode structures. Thus, they did not really resolve the critical issues from the electrode side and, as a result, showed unsatisfactory electrochemical performances.

Received: July 9, 2013

Revised: August 17, 2013

Published: August 27, 2013



Experimental procedures are schematically illustrated in Figure 1. First, 1D polyacrylonitrile (PAN) nanofibers were

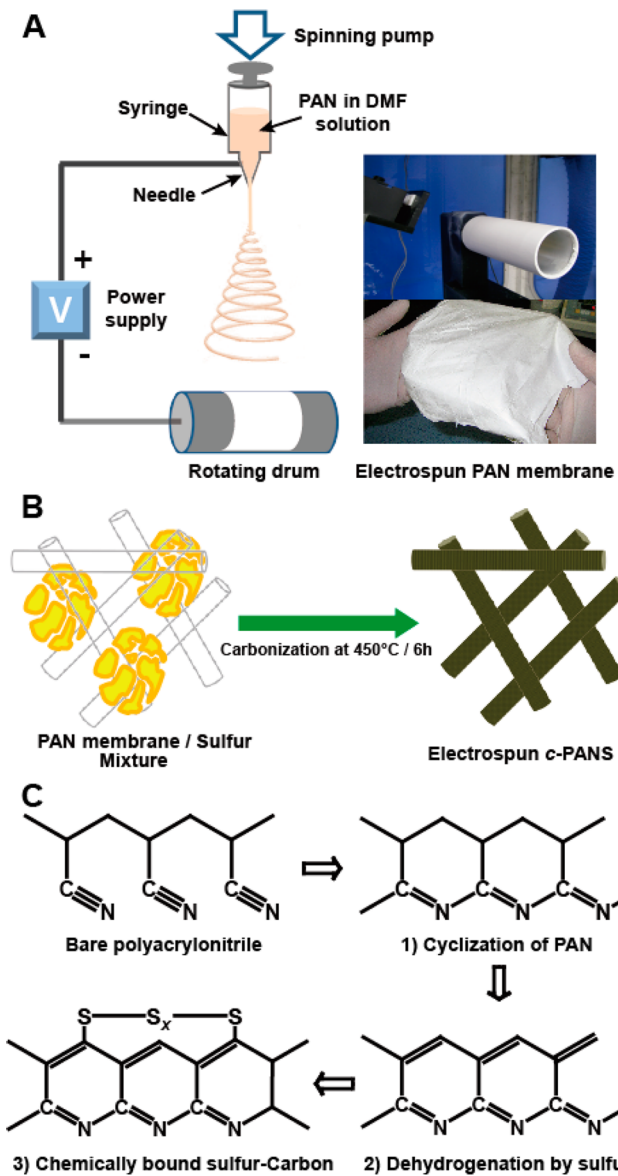


Figure 1. Schematic illustration of experimental procedures for the PAN-derived carbon–sulfur composite with a 1D fibrous structure. (A) An electrospinning process for generation of PAN nanofibers. (B) Carbonization and sulfurization processes by an annealing step at 450 °C. (C) Structural changes during carbonization and sulfurization of c-PANS.

created by an electrospinning process (Figure 1A). The electrospinning technique has been used for a variety of applications including filtration and textile manufacturing because a large quantity of 1D nanostructures can be produced with fine controls of diameter and composition.^{12–14} In the present experiment, the electrospinning process was optimized such that the diameters of the PAN nanofibers (NFs) were quite uniform around 160 nm (Figure S1, Supporting Information). Then, the PAN NFs were thoroughly mixed with elemental sulfur powder in a mass ratio of 20:80, and the mixture underwent a heat treatment at 450 °C for 6 h under nitrogen flow, completing the PAN-derived C–S composite with 1D fibrous structures (Figure 1B). Detailed experimental

procedures are described in the Supporting Information. During the thermal treatment of the PAN and sulfur mixture, it is anticipated that the compound composed of π -conjugated ring structures covalently bonded to sulfur species is formed through three major chemical reactions (Figure 1C): (1) the cyclization of PAN resulting from bond-cleavage of nitrile groups and subsequent bonding of the cleaved nitrogen to the carbon in the neighboring groups.^{15–18} (2) This cyclization is accompanied with dehydrogenation by reaction with sublimed sulfur, resulting in π -conjugated main-chains in conjunction with generation of H₂S as a byproduct.^{15,18–20} (3) At relatively high temperatures, elemental sulfur (S₈) is subject to being cleaved into sulfur-free radicals, which readily undergo reactions with the PAN-derived carbon matrix, forming the final C–S composite structure in which sulfur has been known to form covalent bonds with the carbon atoms in the PAN-derived carbon matrix or sulfur nanodomains consisting of sulfur atom chains with various lengths.^{21–23} These atomic arrangements of sulfur in the carbon matrix play critical roles in stable cycling of the present C–S composite and will be discussed in detail in the paragraphs covering the electrochemical properties.

Scanning electron microscopy (SEM) and transmission electron microscopy (TEM) characterizations were performed to investigate the morphologies of the sulfurized PAN fibers (Figure 2A and B). We denote this carbonized sample as *c*-

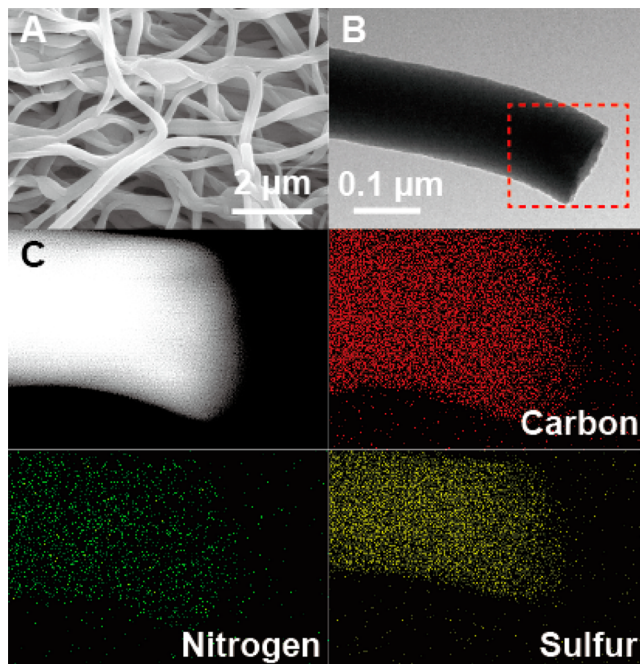


Figure 2. Characterization of electrospun c-PANS NFs. (A) An SEM image of the c-PANS NFs and (B) a TEM image of a single c-PANS NF. (C) STEM images with EDAX elemental mapping for carbon, nitrogen, and sulfur for the spot marked in B.

PANS for convenience. While it was confirmed that the 1D fibrous morphology was preserved during the carbonization/sulfurization steps, the average diameter of the c-PANS NFs is about 150 nm, and the value is approximately 10% smaller than those of the bare PAN NFs (Figure S1, Supporting Information). From TEM characterization of multiple c-PANS NFs ($N = 12$) on the single NF scale (Figure 2B), it was observed that the c-PANS NFs are in highly dense forms, as they did not show conspicuous contrast indicative of void

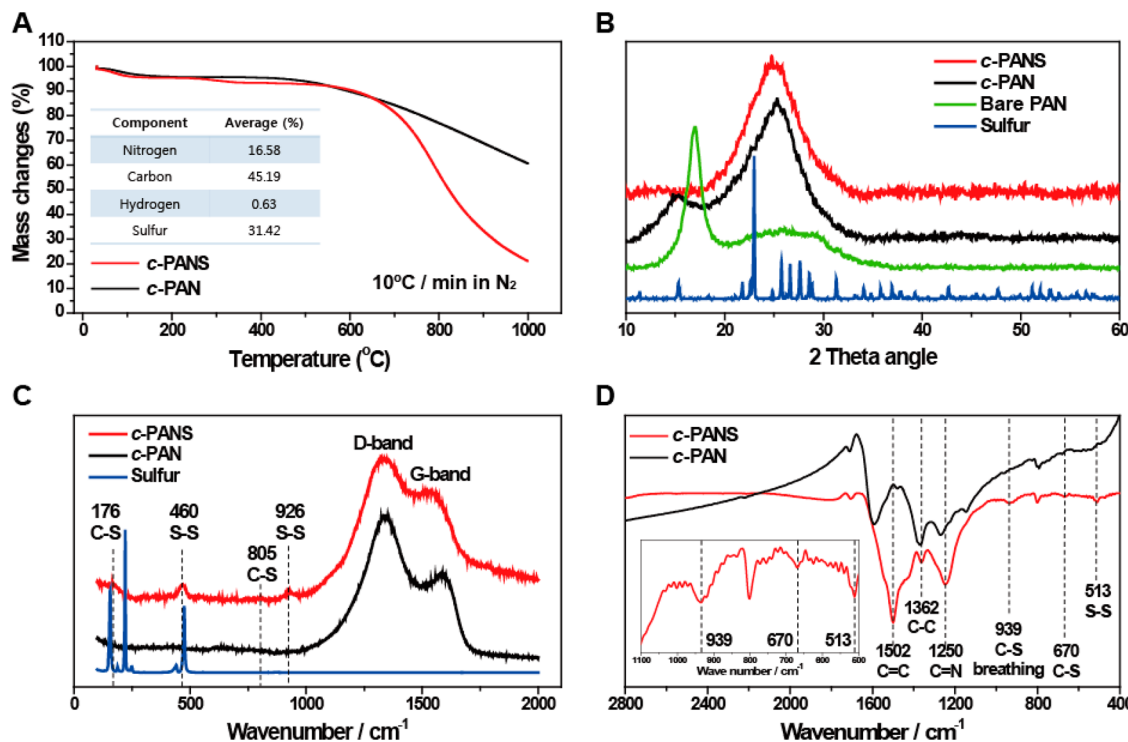


Figure 3. (A) TGA profiles for *c*-PANS (red) and *c*-PAN (black). (A, inset) Summarized elemental contents of *c*-PANS with regard to nitrogen, carbon, and sulfur. (B) XRD patterns of *c*-PANS, *c*-PAN, bare PAN, and elemental sulfur. (C) Raman and (D) FT-IR spectra of *c*-PANS and *c*-PAN. (D, inset) An enlarged FT-IR spectrum of *c*-PANS in the low wavenumber range of 500–1100 cm^{-1} .

space. As shown in Figure 2C, scanning transmission electron microscopy (STEM) and energy-dispersive X-ray spectroscopy (EDAX) were used for elemental mapping of the selected area in Figure 2B. This elemental mapping indicates that all of the elements (carbon, nitrogen, sulfur) are uniformly distributed over the NF and thus verifies that the sulfurization reaction took place thoroughly over the *c*-PANS NFs.

To assess the thermal stability of the *c*-PANS NFs, thermogravimetric analysis (TGA) was carried out in the temperature range of 25–1000 °C (Figure 3A). The carbonized bare PAN without sulfurization (denoted as *c*-PAN) was also analyzed as a control sample. In the temperature range up to 650 °C, both samples exhibited ~3.6% weight loss around 100 °C due to moisture evaporation. The *c*-PANS exhibited an additional 2.2% weight loss around 300 °C, which is ascribed to sublimation of the unreacted sulfur. More significant and also distinctive weight loss was observed in the higher temperature of 650–1000 °C. The weight loss in this temperature range was 77.91% and 38.63% for *c*-PANS and *c*-PAN, respectively. The larger weight loss of *c*-PANS at high temperatures is attributed to sublimation of sulfur species that are chemically bonded and confined in the PAN-derived turbostratic carbon matrix.²⁴ Also, these phenomena can be understood by the bond dissociation energy. The bond dissociation energy (348 kJ/mol) of the C–C bond is substantially larger than those of the C–S bond (272 kJ/mol) and the S–S bond (251 kJ/mol). An elemental analysis (EA) indicates that *c*-PANS consists of 16.58 wt % of nitrogen, 45.19 wt % of carbon, and 31.42 wt % of sulfur (Figure 3A inset). Given that a very minor amount of elemental sulfur was detected in the TGA, this substantial sulfur content implies that the majority of sulfur is strongly bound in the carbon matrix, and *c*-PANS is thermally stable. In an effort to increase the sulfur content and thus the specific capacity of the

electrode, we have also heat-treated samples at lower temperatures following the previous reports.^{21–23} The sample heat-treated at 330 °C showed an increased sulfur content of 48 wt %, but its electrochemical performance turned out to be inferior, indicating that there exists a trade-off between the sulfur content and electrochemical performance, and preservation of the sulfur content below a certain level is crucial for good battery performance.

Figure 3B shows the XRD patterns of elemental sulfur, bare PAN, *c*-PAN, and *c*-PANS. While bare PAN exhibited a major peak at $2\theta = 17^\circ$ corresponding to the (110) plane of the PAN crystal structure,^{25,26} in the case of *c*-PANS, such signature peak of bare PAN disappeared and a broad diffraction peak at $2\theta = 24.4^\circ$ corresponding to the graphitic (002) plane newly appeared, verifying the carbonization of bare PAN. Also, in spite of the presence of the substantial amount of sulfur (~31.42 wt %), the signature peaks of elemental sulfur were not observed for *c*-PANS, indicating that the embedded sulfur exists in smaller molecular forms than S_8 and therefore loses the structural character of the orthorhombic S_8 . The embedded sulfur also lost the crystallinity as evidenced by the broad XRD peaks of *c*-PANS. By contrast, *c*-PAN exhibited a small peak at $2\theta = 15^\circ$, which can be interpreted as a peak-shift of the signature peak of bare PAN at $2\theta = 17^\circ$. The presence of this peak in *c*-PAN suggests that the carbonization of PAN generates a lower degree of turbostratic carbon structure in comparison with that of *c*-PANS, as the XRD spectrum of *c*-PANS did not show any residual PAN signature peaks in this 2θ range. In the case of *c*-PANS, the dehydrogenation process during the reaction with sulfur facilitates intermolecular cross-linking and thus higher degree graphitization.²⁵

The chemical bonds in *c*-PANS were characterized further using Raman spectroscopy and Fourier-transform infrared

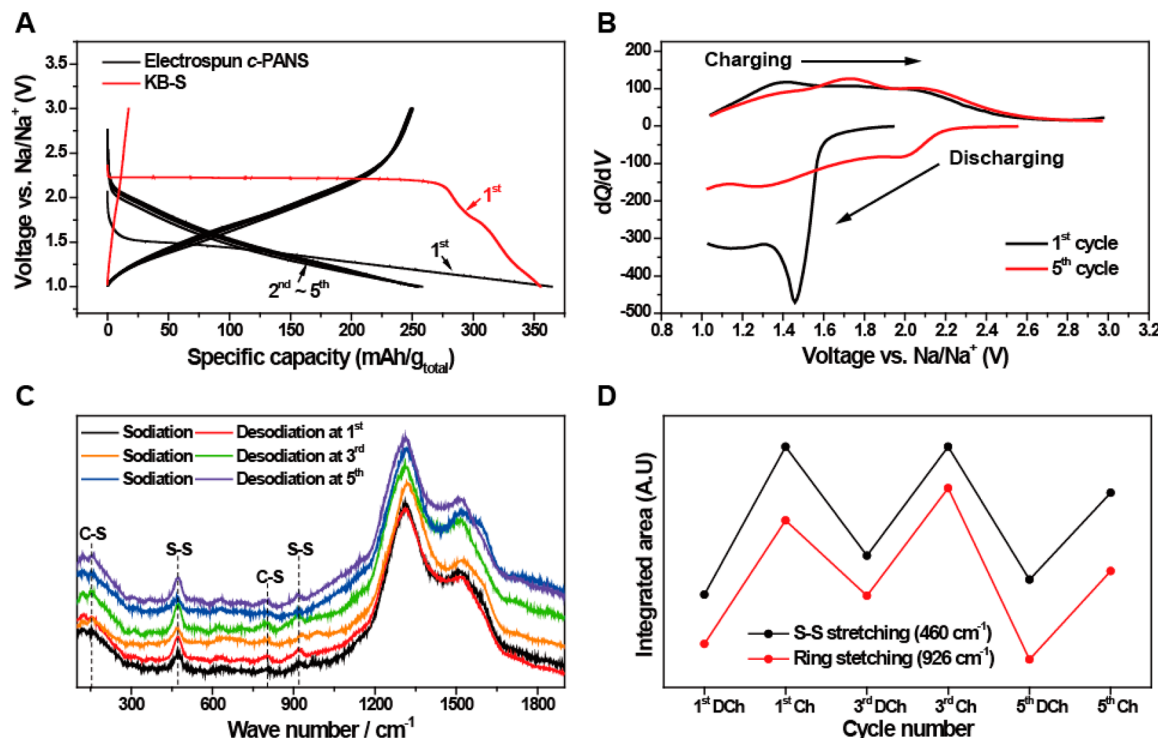


Figure 4. (A) Electrochemical discharge and charge curves of *c*-PANS during the first five cycles and KB-S during the first cycle. The tests were performed at 0.1C (25 mA/g_{total}) for both charge and discharge in the potential range of 1–3 V vs Na/Na⁺. (B) dQ/dV curves of *c*-PANS corresponding to the galvanostatic profiles shown in A. (C) Ex-situ Raman characterization of *c*-PANS at the fully sodiated and desodiated states at the 1st, 3rd, and 5th cycles. (D) Variations of the integrated areas for the ex-situ Raman peaks at 460 and 926 cm⁻¹ corresponding to the S–S stretching and the ring stretching containing S–S bond. The fluctuations reflect the repeated cleavage and dimerization of the S–S bonds during cycling. “Ch” and “DCh” denote charge and discharge, respectively.

spectroscopy (FT-IR). Figure 3C shows Raman spectra of elemental sulfur, *c*-PAN, and *c*-PANS. While elemental sulfur exhibited the well-known three peaks at 150, 217, and 471 cm⁻¹, *c*-PANS showed clearly distinctive peaks at 176, 460, 805, and 926 cm⁻¹. These peaks did not appear in the spectrum of *c*-PAN, indicating that atomic configuration of *c*-PANS became changed markedly after the reaction with elemental sulfur. Based on the previous reports, the peaks located at 176 and 805 cm⁻¹ correspond to the C–S stretch and those at 460 and 926 cm⁻¹ correspond to the S–S stretch.^{21,22} Furthermore, the Raman spectra provide information on the degree of crystallinity of each sample.²⁷ It has been known that typical Raman spectra of carbonaceous materials show two major peaks at 1350 and 1580 cm⁻¹, corresponding to the disorder-induced D band and the graphitic G band, respectively.²⁸ From the intensity ratio (I_G/I_D) of these two bands, *c*-PANS turned out to hold a higher crystallinity than that of *c*-PAN, as the ratios for *c*-PANS and *c*-PAN are 0.85 and 0.61, respectively. This trend reconfirms that the effect of the sulfurization reaction on the formation of turbostratic carbon configuration via dehydrogenation and efficient π – π stacking, which is also consistent with the XRD results.

Figure 3D shows the FT-IR spectra of *c*-PANS and *c*-PAN. The most distinctive signals were observed in the low wavenumber region of 500–1100 cm⁻¹. On the contrary to *c*-PAN, *c*-PANS exhibited the peaks at 513, 670, and 939 cm⁻¹ (Figure 3D inset), although the intensities of these peaks are relatively weak. The peaks at 513 and 670 cm⁻¹ correspond to the S–S stretching and the C–S stretching, respectively. Also, the peak at 939 cm⁻¹ corresponds to the ring breathing in which a C–S bond is contained.^{21,22} Hence, these peaks verify

the formation of C–S and S–S bonds after the sulfurization reaction. Also, the FT-IR results give information on the atomic configuration of the carbon matrix. It has been known that the peaks at 1502 and 1250 cm⁻¹ of *c*-PANS correspond to the symmetric stretching of C=C and C=N bonds, respectively,^{21,22} and the peak at 802 cm⁻¹ corresponds to the ring breathing of hexahydring-rings.^{21,22} The significantly intensified peaks of *c*-PANS at 1502 and 1250 cm⁻¹ compared to those of *c*-PAN are aligned well with the XRD and Raman results that showed the higher degree of turbostratic carbon formation via the dehydrogenation step. Also, it is noteworthy that ¹³C NMR technique is not proper for characterization of the C–S bonds in *c*-PANS because the chemical shift of the C–S bond would be buried by that of the C–C bond in the δ range of 1–3 ppm.^{21,22}

The electrochemical properties of *c*-PANS and *c*-PAN were evaluated by preparing coin-type half-cells. The sodium metal disks and 0.8 M NaClO₄ in ethylene carbonate (EC)–diethyl carbonate (DEC) (1:1 = v/v) were used as the counter/reference electrodes and electrolyte, respectively. The potential ranges were set to 1–3 V vs Na/Na⁺ in all of electrochemical tests. See the Supporting Information for detailed experimental procedures. To compare the electrochemical stability of *c*-PANS with conventional sulfur electrodes, a ketjen black-sulfur composite (denoted as KB-S) was also prepared as a control sample. For this sample, ketjen black and sulfur were mixed in a weight ratio of 20:80, and the mixture was then heat-treated at 155 °C for 12 h. From the voltage profiles of *c*-PANS and KB-S in the first cycles and their differential capacity plots (dQ/dV) in conjunction with ex-situ Raman spectroscopy analyses, the following points are noteworthy.

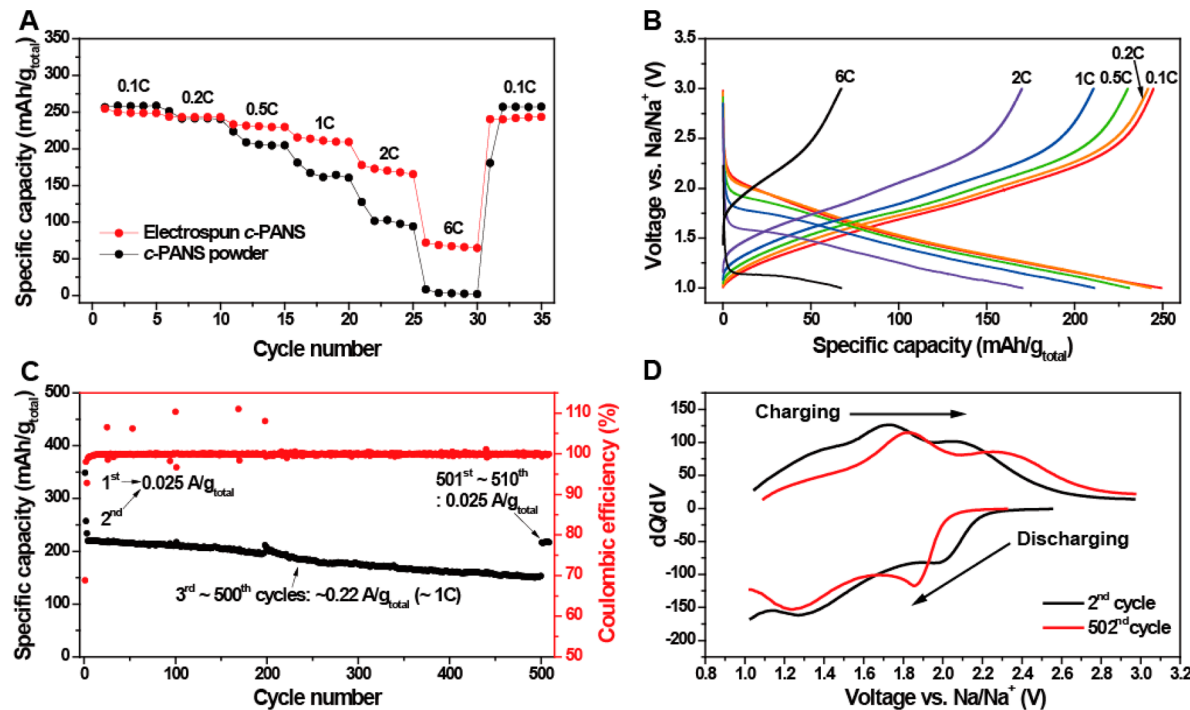


Figure 5. (A) Rate performances of the electrospun c-PANS NFs and c-PANS powder measured at various C-rates. The C-rates were same for both charge and discharge in each cycle. (B) The corresponding potential profiles of c-PANS NFs. (C) Capacity retention and Coulombic efficiencies of c-PANS NFs. The sample was measured at a low C-rate of 0.1C ($0.025\text{ A/g}_{\text{total}}$) in the first two and final ten cycles, but at a higher C-rate of 1C ($0.22\text{ A/g}_{\text{total}}$) in the cycle range of 3–500. (D) The dQ/dV curves at the 2nd and 502nd cycles.

First, as shown in Figure 4A, both c-PANS and KB-S exhibited clearly distinctive galvanostatic profiles in their first cycles when cycled at a C-rate of 0.1C (25 mA/g_{total}). c-PANS showed redox activity as sloping profiles (black lines) in the potential range of 1.0–2.0 V vs Na/Na⁺ while delivering a reversible capacity of 251 mAh/g_{total}. This capacity value is substantially larger than the highest value of the conventional metal oxide-based one: ~195 mAh/g from $\text{Na}_x\text{Fe}_{1/2}\text{Mn}_{1/2}\text{O}_2$.²⁹ By contrast, KB-S (red line) showed a clear plateau in the first discharge (sodiation) around 2.25 V with a capacity of 355 mAh/g, but the most of the capacity disappeared in the subsequent charge. It is speculated that such irreversible behavior of KB-S is originated from the use of the carbonate-based electrolyte because from analogous cases of lithium sulfur battery,^{30,31} lithium polysulfides were found to react with carbonate-based electrolyte solvents, turning into electrochemically inactive chemical products.³⁰ As shown in an SEM image and an XRD result of KB-S composite (Figure S2, Supporting Information), sulfur was coagulated throughout the surfaces of the ketjen black and recrystallized to the orthorhombic crystal structure. To prevent such irreversible behavior, other less reactive solvents such as co-solvents^{32–37} of 1,3-dioxolane (DOL) and 1,2-dimethoxyethane (DME) and tetra(ethylene glycol) dimethyl ether (TEGDME)^{8,38–40} have been adopted for similar sulfur electrodes in Li–S batteries. Hence, it is remarkable that c-PANS overcomes the polysulfide dissolution and exhibited reversible behavior even when the carbonate-based electrolyte was used. This phenomenon is the first indication that the sulfur atoms in c-PANS are strongly bound and confined within the turbostratic carbon matrix, which should be crucial for robust battery performance. The voltage profiles of c-PNAS are also distinctive compared to those of the aforementioned previous room temperature Na–S cells.^{49–51}

based on the elemental sulfur. Similarly to the Li–S batteries,^{8,32–44} the Na–S cells based on the elemental sulfur showed two voltage plateaus in which the upper and lower plateaus are, respectively, related to the formation of long-chain polysulfides (Na_2S_n , $n > 4$) and short-chain ones (Na_2S_n , $n \leq 3$) such as Na_2S_3 ($\Delta G_f = -403.6\text{ kJ/mol}$, $E_o = 2.09\text{ V}$), Na_2S_2 ($\Delta G_f = -378.4\text{ kJ/mol}$, $E_o = 1.96\text{ V}$), and Na_2S ($\Delta G_f = -354.6\text{ kJ/mol}$, $E_o = 1.84\text{ V}$).

Second, the distinctive profiles of c-PANS are more clearly unburied in dQ/dV plots (Figure 4B). While c-PANS exhibited a single cathodic peak at a relatively low voltage of 1.45 V vs Na/Na⁺ in the first discharging, in the subsequent discharging, two cathodic peaks with smaller intensities appeared around 1.28 and 2.05 V. Such different behavior is likely to be related to atomic environments of sulfur species. In c-PANS, it is anticipated that the embedded sulfur exists in small molecular states with chemical bonding to the PAN-derived carbon matrix. Thus, additional activation processes, such as C–S bond cleavage and rearrangement of sulfur atoms, appear to be required for initial reaction with Na ions, resulting in the downshift of the voltage plateau in the first cycle. In other words, once sulfur atoms are activated by certain atomic rearrangements in the first cycle, their reactions with Na ions require lower energy barriers to overcome, therefore upshifting voltage plateaus in the subsequent cycles. However, some variations in the sulfur chain length and atomic environment are created during such atomic rearrangements in the first cycle, and those variations turned out as relatively less well-defined plateaus in the subsequent cycles. In particular, the two distinctive peaks in dQ/dV reflect different reaction mechanisms with Na ions.^{15,18,21–23,45} The higher peak (2.05 V during discharging at the fifth cycle) is reflective of the Na ion reaction with sulfur domains isolated from the carbon matrix.

By contrast, the lower peak (1.28 V during discharging at the fifth cycle) is reflective of the Na ion reaction with sulfur atoms bonded to the carbon matrix via namely the repeated electrodimerization/scission process.^{21–23,45}

Third, the bonding character of *c*-PANS during the reaction with Na ions was clarified further by ex-situ Raman characterization (Figure 4C). The cleavage of disulfide bonds during sodiation and their redimerization during desodiation, that is, the latter reaction mechanism in the previous paragraph, were detected and verified by fluctuating peak intensities in each cycle (Figure 4D). The peak at 926 cm^{-1} corresponding to the ring stretching containing the S–S bond decreased during sodiation reflecting the cleavage of disulfide bonds, but vice versa during the reversed situation of desodiation. Similarly, the peak at 460 cm^{-1} corresponding to the S–S stretching also fluctuates during each cycle, again indicating the cleavage and reconstruction of S–S bonds by the aforementioned two mechanisms.

Finally, *c*-PANS showed the first discharging/charging capacities of $364/250\text{ mAh/g}_{\text{total}}$ ($1158\text{ and }796\text{ mAh/g}_{\text{sulfur}}$) with a Coulombic efficiency (CE) of 68.7%. This reversible capacity of *c*-PANS is substantially larger than those of the previous room-temperature Na–S cells^{4,9–11} as well as other existing metal oxide materials.²⁹ Once again, such superior capacity of *c*-PANS is a combined outcome from its unique structure: the turbostratic carbon matrix supports decent electric conductivity, while the sulfur atoms occupying a large portion of the entire active material (~31 wt %) are stably bound to the carbon matrix. Also, the CE improved as the cycling proceeded. For instance, the CE reached 98.8% in the fifth cycle with the discharging/charging capacities of $253/250\text{ mAh/g}_{\text{total}}$ ($805\text{ and }796\text{ mAh/g}_{\text{sulfur}}$). The successively increasing CEs for a larger number of cycles will be described further in the paragraph discussing on the cycling performance. The low first CE may be associated with the PAN-derived carbon matrix that gives rise to irreversible side reactions, which was indeed confirmed in our control experiment with *c*-PAN (Figure S3, Supporting Information). *c*-PAN showed the first CE of 59% (discharging/charging capacities = $32/19\text{ mAh/g}_{\text{total}}$).

Electrospun *c*-PANS showed excellent rate performance especially compared to that of the case without any morphological control (Figure 5A and B). The control sample was synthesized through the same process as *c*-PANS, but based on PAN powder instead of PAN NFs. The control sample showed spherical morphologies with $1\text{--}10\text{ }\mu\text{m}$ dimensions (Figure S4, Supporting Information). For the rate tests, various current rates were applied from 0.1C to 6C ($0.025\text{ A/g}_{\text{total}}$ to $1.5\text{ A/g}_{\text{total}}$). In each cycle, the rates were the same for both charge and discharge. Even though both samples showed similar rate performances at low C-rates of $0.1\text{--}0.2\text{C}$ ($0.025\text{--}0.050\text{ A/g}_{\text{total}}$), the *c*-PANS NFs exhibited superior rate performance at higher C-rates. *c*-PANS NFs showed better capacity retentions, such as 94% at 0.5C ($0.125\text{ A/g}_{\text{total}}$), 87% at 1C ($0.250\text{ A/g}_{\text{total}}$), and 72% at 2C ($0.500\text{ A/g}_{\text{total}}$). In particular, when the current rate increased 60 times corresponding to 6C ($1.5\text{ A/g}_{\text{total}}$), the sample showed discharge capacity of $72\text{ mAh/g}_{\text{total}}$ but the counterpart showed almost no discharge capacity. Such superior rate capabilities are associated with the 1D fibrous nanostructure with smaller dimensions that facilitate efficient diffusion of Na ions during charge and discharge. Also, in the chemical structure viewpoint, since sulfur chains or domains are covalently bonded to the

conjugated turbostratic carbon matrix containing nitrogen atoms with excess electrons, *c*-PANS can support efficient electron transfer, which is in contrast with conventional sulfur electrodes suffering from low electronic conductivities.^{15,18,21,22}

Figure 5C shows cycling performance of the *c*-PANS NFs when cycled at a low C-rate of 0.1C ($0.025\text{ A/g}_{\text{total}}$) for the first two cycles and at a higher C-rate of 1C ($0.22\text{ A/g}_{\text{total}}$) for the rest of the cycles. Discharge and charge currents were the same in each cycle during the entire cycling test. Unlike typical Li–S and Na–S batteries suffering from limited cycle lives due to low electronic conductivity of sulfur and dissolution of intermediate lithium (or sodium) polysulfides,^{4,33–37} *c*-PANS NFs showed excellent cycling performance such that 70% ($153\text{ mAh/g}_{\text{total}}$) of the capacity ($219\text{ mAh/g}_{\text{total}}$) in the fifth cycle was retained even after 500 cycles. The CE reached 99.93% at the 500th cycle, and the average CE in the cycling range of 3–500 is 99.84%. This good cycling performance suggests that the sulfur species in *c*-PANS stay robust within the PAN-derived matrix during repeated (de)sodiation while preventing the fatal issues of the conventional Li–S and Na–S cells. To confirm the electrochemical stability, after 500 cycles, *c*-PANS NFs were tested again at the initial 0.1C rate. When plotted in dQ/dV , the profiles at the second and 502nd cycles match well with each other, although higher overpotentials were observed at the 502nd cycle perhaps due to increased interfacial resistances (Figure 5D). The two redox peaks (1.85 and 1.25 V during discharge @502nd cycle) associated with the aforementioned two reaction mechanisms were still observed.

To verify the significantly reduced dissolution of sodium polysulfides, the sodium–metal counter electrodes were characterized using SEM and EDAX elemental analyses (Figure 6) without any washing step involved. As displayed in an SEM

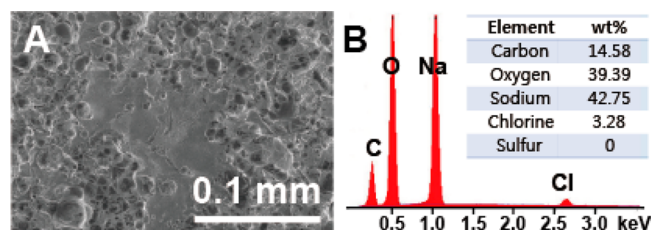


Figure 6. (A) An SEM image of the surface of the sodium metal counter electrode after 500 cycles. (B) Elemental information obtained by EDAX characterization for the entire area shown in A.

image taken after 500 cycles (Figure 6A), some cracks and irregular pores were frequently observed on the surface of the sodium metal counter electrode. When elemental analyses (Figure 6B and Figure S5, Supporting Information) were conducted over the area ($250 \times 170\text{ }\mu\text{m}^2$) shown in Figure 6A, sulfur was not detected at all, confirming the suppressed dissolution of sodium polysulfides from the *c*-PANS NFs.

In conclusion, we have demonstrated a highly robust Na–S battery operating at room temperature, which is in contrast to the conventional counterparts working at high temperatures using the melt active materials. The underlying origin of the robust electrochemical behavior is the stable atomic configuration of sulfur in the carbonized PAN matrix that resolves the fatal issues of the conventional Li–S batteries: dissolution of polysulfide compounds and low conductivity of elemental sulfur. Additionally, the 1D fibrous structures with $\sim 150\text{ nm}$ diameters facilitate improved kinetics for (de)sodiation. The

superior electrochemical performance and simple synthesis of the given *c*-PANS electrode must be a meaningful step in SIB research and its progress toward for emerging large-scale energy storage.

■ ASSOCIATED CONTENT

Supporting Information

Experimental procedures and additional physical/electrochemical characterization. This material is available free of charge via the Internet at <http://pubs.acs.org>.

■ AUTHOR INFORMATION

Corresponding Author

*E-mail: jangwookchoi@kaist.ac.kr.

Notes

The authors declare no competing financial interest.

■ ACKNOWLEDGMENTS

We acknowledge the financial support by the National Research Foundation of Korea (NRF) grant funded by the Korea government (MEST) (NRF-2010-C1AAA001-0029031 and NRF-2012-R1A2A1A01011970).

■ REFERENCES

- (1) Oshima, T.; Kajita, M.; Okuno, A. *Int. J. Appl. Ceram. Technol.* **2004**, *1* (3), 269–276.
- (2) Wen, Z. Y.; Cao, J. D.; Gu, Z. H.; Xu, X. H.; Zhang, F. L.; Lin, Z. X. *Solid State Ionics* **2008**, *179* (27–32), 1697–1701.
- (3) Hueso, K. B.; Armand, M.; Rojo, T. *Energy Environ. Sci.* **2013**, *6* (3), 734–749.
- (4) Park, C. W.; Ahn, J. H.; Ryu, H. S.; Kim, K. W.; Ahn, H. J. *Electrochem. Solid-State Lett.* **2006**, *9* (3), A123–A125.
- (5) Palomares, V.; Serras, P.; Villaluenga, I.; Hueso, K. B.; Carretero-Gonzalez, J.; Rojo, T. *Energy Environ. Sci.* **2012**, *5* (3), 5884–5901.
- (6) Ellis, B. L.; Nazar, L. F. *Curr. Opin. Solid State Mater. Sci.* **2012**, *16* (4), 168–177.
- (7) Mikhaylik, Y. V.; Akridge, J. R. *J. Electrochem. Soc.* **2004**, *151* (11), A1969–A1976.
- (8) Ji, X. L.; Lee, K. T.; Nazar, L. F. *Nat. Mater.* **2009**, *8* (6), 500–506.
- (9) Ryu, H.; Kim, T.; Kim, K.; Ahn, J. H.; Nam, T.; Wang, G.; Ahn, H. J. *J. Power Sources* **2011**, *196* (11), 5186–5190.
- (10) Park, C. W.; Ryu, H. S.; Kim, K. W.; Ahn, J. H.; Lee, J. Y.; Ahn, H. J. *J. Power Sources* **2007**, *165* (1), 450–454.
- (11) Kim, J. S.; Ahn, H. J.; Kim, I. P.; Kim, K. W.; Ahn, J. H.; Park, C. W.; Ryu, H. S. *J. Solid State Electrochem.* **2008**, *12* (7–8), 861–865.
- (12) Greiner, A.; Wendorff, J. H. *Angew. Chem., Int. Ed.* **2007**, *46* (30), 5670–5703.
- (13) Li, D.; Xia, Y. N. *Adv. Mater.* **2004**, *16* (14), 1151–1170.
- (14) Huang, Z. M.; Zhang, Y. Z.; Kotaki, M.; Ramakrishna, S. *Compos. Sci. Technol.* **2003**, *63* (15), 2223–2253.
- (15) Wang, J. L.; Yang, J.; Wan, C. R.; Du, K.; Xie, J. Y.; Xu, N. X. *Adv. Funct. Mater.* **2003**, *13* (6), 487–492.
- (16) Rahaman, M. S. A.; Ismail, A. F.; Mustafa, A. *Polym. Degrad. Stab.* **2007**, *92* (8), 1421–1432.
- (17) Guo, J. C.; Yang, Z. C.; Yu, Y. C.; Abruna, H. D.; Archer, L. A. *J. Am. Chem. Soc.* **2013**, *135* (2), 763–767.
- (18) Wang, J. L.; Yang, J.; Xie, J. Y.; Xu, N. X. *Adv. Mater.* **2002**, *14* (13–14), 963–965.
- (19) Yin, L. C.; Wang, J. L.; Lin, F. J.; Yang, J.; Nuli, Y. *Energy Environ. Sci.* **2012**, *5* (5), 6966–6972.
- (20) Yin, L. C.; Wang, J. L.; Yang, J.; Nuli, Y. N. *J. Mater. Chem.* **2011**, *21* (19), 6807–6810.
- (21) Yu, X. G.; Xie, J. Y.; Yang, J.; Huang, H. J.; Wang, K.; Wen, Z. S. *J. Electroanal. Chem.* **2004**, *573* (1), 121–128.
- (22) Yu, X. U.; Xie, J. Y.; Li, Y.; Huang, H. J.; Lai, C. Y.; Wang, K. J. *Power Sources* **2005**, *146* (1–2), 335–339.
- (23) Fanous, J.; Wegner, M.; Grimminger, J.; Andresen, A.; Buchmeiser, M. R. *Chem. Mater.* **2011**, *23* (22), 5024–5028.
- (24) Chang, C. H. *Carbon* **1981**, *19* (3), 175–186.
- (25) Yu, M. J.; Xu, Y.; Wang, C. G.; Zhu, B.; Wang, Y. X.; Hu, X. Y.; Lin, X. *J. Appl. Polym. Sci.* **2012**, *124* (6), 5172–5179.
- (26) Kumamaru, F.; Kajiyama, T.; Takayanagi, M. *J. Cryst. Growth* **1980**, *48* (2), 202–209.
- (27) Lee, J. H.; Shin, W. H.; Ryou, M. H.; Jin, J. K.; Kim, J.; Choi, J. W. *ChemSusChem* **2012**, *5* (12), 2328–2333.
- (28) Cuesta, A.; Dhamelincourt, P.; Laureyns, J.; Martinezalonso, A.; Tascon, J. M. D. *Carbon* **1994**, *32* (8), 1523–1532.
- (29) Yabuuchi, N.; Kajiyama, M.; Iwatake, J.; Nishikawa, H.; Hitomi, S.; Okuyama, R.; Usui, R.; Yamada, Y.; Komaba, S. *Nat. Mater.* **2012**, *11* (6), 512–517.
- (30) Gao, J.; Lowe, M. A.; Kiya, Y.; Abruna, H. D. *J. Phys. Chem. C* **2011**, *115* (50), 25132–25137.
- (31) Xin, S.; Gu, L.; Zhao, N. H.; Yin, Y. X.; Zhou, L. J.; Guo, Y. G.; Wan, L. J. *J. Am. Chem. Soc.* **2012**, *134* (45), 18510–18513.
- (32) Yang, Y.; Zheng, G. Y.; Misra, S.; Nelson, J.; Toney, M. F.; Gui, Y. *J. Am. Chem. Soc.* **2012**, *134* (37), 15387–15394.
- (33) Yang, Y.; Yu, G. H.; Cha, J. J.; Wu, H.; Vosgueritchian, M.; Yao, Y.; Bao, Z. A.; Cui, Y. *ACS Nano* **2011**, *5* (11), 9187–9193.
- (34) Su, Y. S.; Manthiram, A. *Nat. Commun.* **2012**, *3*, 1166.
- (35) Schuster, J.; He, G.; Mandlmeier, B.; Yim, T.; Lee, K. T.; Bein, T.; Nazar, L. F. *Angew. Chem., Int. Ed.* **2012**, *51* (15), 3591–3595.
- (36) Seh, Z. W.; Li, W. Y.; Cha, J. J.; Zheng, G. Y.; Yang, Y.; McDowell, M. T.; Hsu, P. C.; Cui, Y. *Nat. Commun.* **2013**, *4*, 1331.
- (37) Evers, S.; Yim, T.; Nazar, L. F. *J. Phys. Chem. C* **2012**, *116* (37), 19653–19658.
- (38) Kim, J.; Lee, D. J.; Jung, H. G.; Sun, Y. K.; Hassoun, J.; Scrosati, B. *Adv. Funct. Mater.* **2013**, *23* (8), 1076–1080.
- (39) Cheon, S. E.; Ko, K. S.; Cho, J. H.; Kim, S. W.; Chin, E. Y.; Kim, H. T. *J. Electrochem. Soc.* **2003**, *150* (6), A796–A799.
- (40) Ji, X. L.; Evers, S.; Black, R.; Nazar, L. F. *Nat. Commun.* **2011**, *2*, 325.
- (41) Zhang, C. F.; Wu, H. B.; Yuan, C. Z.; Guo, Z. P.; Lou, X. W. *Angew. Chem., Int. Ed.* **2012**, *51* (38), 9592–9595.
- (42) Wang, H. L.; Yang, Y.; Liang, Y. Y.; Robinson, J. T.; Li, Y. G.; Jackson, A.; Cui, Y.; Dai, H. J. *Nano Lett.* **2011**, *11* (7), 2644–2647.
- (43) Zheng, G. Y.; Yang, Y.; Cha, J. J.; Hong, S. S.; Cui, Y. *Nano Lett.* **2011**, *11* (10), 4462–4467.
- (44) Lee, K. T.; Black, R.; Yim, T.; Ji, X. L.; Nazar, L. F. *Adv. Energy Mater.* **2012**, *2* (12), 1490–1496.
- (45) Liang, Y. L.; Tao, Z. L.; Chen, J. *Adv. Energy Mater.* **2012**, *2* (7), 742–769.